

Design of high-pressure iron Rayleigh–Taylor strength experiments for the National Ignition Facility

Cite as: J. Appl. Phys. **131**, 145902 (2022); <https://doi.org/10.1063/5.0084693>

Submitted: 09 January 2022 • Accepted: 27 March 2022 • Published Online: 12 April 2022

 Gaia Righi,  Thomas E. Lockard,  Robert E. Rudd, et al.



View Online



Export Citation



CrossMark

ARTICLES YOU MAY BE INTERESTED IN

[On the transition from weak to strong shock response](#)

Journal of Applied Physics **131**, 145901 (2022); <https://doi.org/10.1063/5.0084553>

[Characterization methods for defects and devices in silicon carbide](#)

Journal of Applied Physics **131**, 140903 (2022); <https://doi.org/10.1063/5.0077299>

[Dynamic response of polycrystalline high energetic systems: Constitutive modeling and application to impact](#)

Journal of Applied Physics **131**, 145101 (2022); <https://doi.org/10.1063/5.0080848>

Lock-in Amplifiers
up to 600 MHz



Zurich
Instruments



Design of high-pressure iron Rayleigh–Taylor strength experiments for the National Ignition Facility

Cite as: J. Appl. Phys. **131**, 145902 (2022); doi: [10.1063/5.0084693](https://doi.org/10.1063/5.0084693)

Submitted: 9 January 2022 · Accepted: 27 March 2022 ·

Published Online: 12 April 2022



View Online



Export Citation



CrossMark

Gaia Righi,^{1,a)} Thomas E. Lockard,² Robert E. Rudd,² Marc A. Meyers,¹ and Hye-Sook Park²

AFFILIATIONS

¹Materials Science and Engineering Program, University of California, San Diego, La Jolla, California 92093, USA

²Lawrence Livermore National Laboratory, Livermore, California 94550, USA

^{a)}Author to whom correspondence should be addressed: grighi@ucsd.edu

ABSTRACT

Iron is an important metal, scientifically and technologically. It is a common metal on Earth, forming the main constituent of the planet's inner core, where it is believed to be in solid state at high pressure and high temperature. It is also the main component of many important structural materials used in quasistatic and dynamic conditions. Laser-driven Rayleigh–Taylor instability provides a means of probing material strength at high pressure and high temperature. The unavoidable phase transition in iron at relatively low pressure induces microstructural changes that ultimately affect its strength in this extreme regime. This inevitable progression can make it difficult to design experiments and understand their results. Here, we address this challenge with the introduction of a new approach: a direct-drive design for Rayleigh–Taylor strength experiments capable of reaching up to 400 GPa over a broad range of temperatures. We use 1D and 2D hydrodynamic simulations to optimize target components and laser pulse shape to induce the phase transition and compress the iron to high pressure and high temperature. At the simulated pressure–temperature state of 350 GPa and 4000 K, we predict a ripple growth factor of 3–10 depending on the strength with minimal sensitivity to the equation of state model used. The growth factor is the primary observable, and the measured value will be compared to simulations to enable the extraction of the strength under these conditions. These experiments conducted at high-energy laser facilities will provide a unique way to study an important metal.

Published under an exclusive license by AIP Publishing. <https://doi.org/10.1063/5.0084693>

I. INTRODUCTION

The study of iron strength at high pressure is a key interest to both the geodynamic physics and materials science communities. In geophysics, understanding the strength and constitutive behavior of iron at the Earth's core pressure and temperature conditions will help to calibrate existing theories of core formation and the geodynamo.¹ The lattice preferred orientation (LPO) of the inner core is strongly influenced by the material's bulk properties and could have major consequences on core rheology.² The higher the iron strength, the longer the time required to form the LPO, possibly altering the timeline of Earth's formation and biogenesis. There is no feasible way to directly probe core conditions (360 GPa, 6000 K, 10^{-8} s⁻¹). However, laser-driven experiments are advantageous in that core pressure and temperature can simultaneously be achieved relatively easily. Therefore, although the experiments described herein occur at much higher strain rates, the scarcity of benchmarks on iron strength

in general drives these investigations that can provide any additional information on deformation behavior of iron at high pressure and temperature. In materials science, it is known that the dependence of iron strength on crystal orientation and polycrystalline texture is significant.³ This type of anisotropic behavior is certainly not new to the field but can help inform on elastic constants and plasticity behavior at the proper pressure/temperature conditions in order to better understand the core anisotropy and constrain core dynamic models. Iron is also the basis for many commonly used structural materials, such as steels and high entropy alloys, and by understanding its extreme behavior, one can begin to systematically investigate more complex ferritic materials at high pressure.

Plastic deformation of metals is a complex process that, as stated by Cottrell, was one of the first to be studied and one of the last to be solved.⁴ The stress that the material can sustain is a function of internal and external parameters. The internal ones are the

multiple levels of the structure, from the nano- to the macro-scale. The external ones are the thermodynamic parameters of pressure, temperature, and the strain rate. Modeling this response is done, at the engineering level, by simple phenomenological equations, such as the Johnson–Cook model.⁵ More fundamental, physically based approaches incorporate a daunting complex of effects, including thermally activation dislocation motion, viscous drag, relativistic effects, and additional contributions from grain size or other imperfections. The Preston–Tonks–Wallace (PTW) model⁶ represents an apex constitutive equation that covers the range of strain rates from 10^{-3} to 10^{12} s^{-1} and is well suited for shock compression. By performing these experiments at extreme conditions, this type of commonly used constitutive equation can be validated in this regime.

Iron poses unique challenges to the design of effective ramp compression experiments that are sensitive to its strength. The structural alpha–epsilon phase transformation occurs at $\sim 5\%$ of the inner core pressure and is unavoidable. It complicates the design in several ways: (i) standard iron strength models developed for the alpha phase cannot be expected to extrapolate well into the epsilon phase for the purposes of design; (ii) this uncertainty is further complicated by likely microstructural changes affecting strength and heating associated with the significant volume collapse, both resulting from the phase transformation; and (iii) the inability of indirect-drive designs to produce a broad range of temperatures at a prescribed pressure. The Rayleigh–Taylor (RT) instability induces material deformation, enabling a method to determine the material's strength when traditional measurement capabilities, such as strain gauges, are inadequate under high-pressure ($>100 \text{ GPa}$) and high strain rate ($>10^7 \text{ s}^{-1}$) conditions. This instability occurs at the interface of two fluids of different densities by virtue of the lighter fluid accelerating into the heavier fluid.^{7,8} RT strength experiments at state-of-the-art laser facilities, such as the Laboratory for Laser Energetics (LLE) and the National Ignition Facility (NIF), have been developed over many years.^{9–11} The growth of RT unstable perturbations for an ideal fluid depends on the Atwood number [$A = (\rho_1 - \rho_2)/(\rho_1 + \rho_2)$, where ρ_1, ρ_2 are densities of the interface materials], acceleration, and perturbation wavelength. This growth can be inhibited in real fluids through a variety of mechanisms: self-radiation,¹² thermal diffusion,^{13–15} convection,¹⁶ ablation,^{17–19} “snow-plow,”²⁰ and viscosity.²¹ Similar to viscosity, the strength of a material can be inferred by comparing the difference between the initial and final perturbation amplitudes.²² If the material has no strength, the ripple growth will be uninhibited and grow at the classical rate; however, if the material has a finite strength, growth will be suppressed. In the linear RT regime, the amount of RT suppression can be used to infer a measure of strength and the ripple growth can be measured by face-on x-ray radiography.

Experiments are being conducted at LLE (using the Omega EP laser²³) and the NIF²⁴ to study iron strength under a variety of conditions of pressure and temperatures using direct-drive (DD) laser shots. For direct-drive experiments, ramp compression is achieved by laser pulse shaping. A new RT campaign at Omega EP is designed to investigate the temperature dependence of iron strength at high pressure (100 GPa). Hohlräum-driven RT experiments at 130 GPa and relatively low temperature found the strength of iron to be $\sim 40 \text{ GPa}$,²² but moderate strain rate shear plate

impact experiments and static diamond anvil cell experiments yield much lower strength.^{25,26} The NIF can achieve higher pressures ($P \sim 350 \text{ GPa}$) and temperatures ($T \sim 5000 \text{ K}$), comparable to Earth and exoplanet interiors. Few experimental studies exist for iron strength at these conditions. Surprisingly, EXAFS results for the plastic-work-induced temperature rise during ramp compression imply an enormously high strength of 60 GPa.²⁷ Other promising techniques, such as *in situ* x-ray diffraction are not yet able to reach suitably high pressures.²⁸ The iron RT experiments currently being conducted at the NIF aim to resolve discrepancies in the literature and determine the strength of iron at the Earth's core P–T conditions. The hohlraum-driven, or indirect-drive, platform is well developed at the NIF^{29–33} and has been used for a few iron RT experiments. Although hohlraum-driven experiments are successful at reaching Earth core pressures, the temperature is significantly lower than desired—about a third of the core temperature. This is because the current hohlraum design was optimized for higher-Z materials, such as tantalum or lead, and, therefore, does not perform as well for iron. Intensive design work could be used to develop this indirect-drive platform for iron, but finer control can be achieved using direct-drive laser pulse shaping so the authors focus on that design work instead. Furthermore, usage of a hohlraum is subject to gold plasma filling in the space where the laser beams ablate the inner walls, resulting in compromised radiography data for low-Z RT experiments, such as iron. These issues have pushed the development of the direct-drive platform in which conditions can be precisely controlled through target design and laser pulse shaping. These DD iron RT experiments are the first of their kind to take advantage of the uniquely adjustable long (60 ns) pulse shape to reach hundreds of GPa and high-temperature conditions. These experimental RT laser campaigns rely on hydrodynamic simulations to design both target and pulse shape for the desired conditions and predict strength. A description of the computational methods is presented in Sec. II. Results for the target design, pulse shape, and the subsequent strength effects are presented in Sec. III.

II. SIMULATION METHODS

Hydrodynamic simulations are designed to solve a set of partial differential equations, which includes the conservation laws (mass, momentum, and energy), equation of state (EOS), radiation transport, and other material phenomena (thermal conductivity, ionization, magnetism, etc.).³⁴ Hydra³⁵ and Ares³⁶ are two such codes that use a structured mesh and arbitrary Lagrange–Eulerian formulation to accurately model radiation transport for a variety of laser experiments. One of the benefits of these codes is that mesh motion can also be solely Lagrangian—where the coordinates of the mesh are tied to the fluid at $t = 0$ and move with the fluid velocity, keeping zone mass constant throughout the simulation. This formulation allows for better modeling of distinct, layered targets as are used in DD shots. The numerical code Hydra³⁵ was used to accurately model laser interaction with an ablator material in one-dimension to create adequate compression profile for the iron sample. Optimizations of the target layers and pulse shape were conducted to minimize temperature gradients while maximizing pressure stability without melting in the iron region. Crucial requirements are for peak pressure to reach 350 GPa, peak

temperature 4000–6000 K, and $T/T_m < 1$, where T_m is the melting temperature (at the prescribed pressure). Ares³⁶ was used in two-dimensions to introduce a sinusoidal pattern onto the front surface of the iron and simulate RT ripple growth with strength. Here and in what follows the “front” is the face from which the compressive wave enters, i.e., the direction of the Be ablator. In each hydrodynamic simulation, different constitutive models were used for the iron such as Steinberg–Guinan³⁷ (SG) and Preston–Tonks–Wallace⁶ (PTW) to determine the effect of strength on ripple growth. Such simulations will be used to compare with experimental data, inferring iron strength at high pressure–temperature conditions.

A. Strength

Strength is a characteristic property of materials and dictates behavior in many applications. At low levels of applied stress, the material lattice simply distorts elastically in a reversible fashion and can return to its original configuration. With increased stress, however, the lattice permanently shifts, and deformation occurs at all levels from the nano- to the macro-scale. The resistance to that deformation is the basis of strength. At large strain rates, the mechanics of deformation becomes complicated. Dislocations, the primary carriers of permanent deformation, are governed by thermal activation at low strain rates and viscous drag and relativistic effects at higher strain rates. Their collective behavior is described by analytical models or through computations. The SG model was first developed in 1980 for high-pressure modeling at high strain rates³⁷ and later (1989) expanded to include strain rate effects and be valid for lower strain rate experiments.³⁸ This is a well-developed formulation that is commonly used for the plastic behavior seen in RT experiments. This semi-empirical model describes shear modulus (G) and yield strength (Y) as a function of strain (ϵ), pressure (P), and temperature (T),

$$G(P, T) = G_0 \left[1 + (G'_p/G_0)P\eta^{-\frac{1}{3}} - (G'_T/G_0)(T - 300 \text{ K}) \right], \quad (1)$$

$$\hat{\tau} = \hat{\tau}_s + \frac{1}{p}(s_0 - \hat{\tau}_y) \ln \left[1 - \left(1 - \exp \left(-p \left(\frac{\hat{\tau}_s - \hat{\tau}_y}{s_0 - \hat{\tau}_y} \right) \right) \right) \right] \times \exp \left(\frac{-p\theta\epsilon}{(s_0 - \hat{\tau}_y) \left(\exp \left(p \left(\frac{\hat{\tau}_s - \hat{\tau}_y}{s_0 - \hat{\tau}_y} \right) \right) - 1 \right)} \right), \quad (4)$$

where $\hat{\tau}_s$ and $\hat{\tau}_y$ are the work hardening saturation stress and the yield stress, which are functions of temperature, strain rate, and shear modulus; p and θ (from the Voce relation⁴⁰) are material parameters, and s_0 is the value that $\hat{\tau}_s$ takes at zero temperature. Equation (4) is accurate for many metals in the thermal activation regime when the strain rate is below 10^9 s^{-1} . Above that strain rate, the high temperature and large strains associated with a strong shock causes work hardening to be saturated.⁶ At this condition, $\hat{\tau}_s = \hat{\tau}_y = s_0(\dot{\psi}/\gamma\xi)^\beta$, where $\dot{\psi}$ is the plastic strain rate, γ is a dimensionless material parameter, ξ is the atomic vibration

$$Y = Y_{wh} \frac{G(P, T)}{G_0}, \quad (2)$$

where G_0 is the shear modulus at reference conditions, $\eta = \rho/\rho_0$ is the compression ratio in density, and G'_p and G'_T are the pressure and temperature dependence coefficients for the shear modulus. The work-hardened yield strength, Y_{wh} , is defined by

$$Y_{wh} = Y_0 [1 + \beta(\epsilon_i + \epsilon_p)]^n, \quad (3)$$

where Y_0 is yield strength at reference conditions, ϵ_p and ϵ_i are the deformed and initial equivalent plastic strain, and β and n are work hardening parameters. If Y_{wh} exceeds the maximum yield strength, $Y_{wh, max}$, then Y_{wh} is reset to $Y_{wh, max}$. In the simulations presented here, multipliers of this SG model are also used to predict a range of strength by multiplying Y_0 and $Y_{wh, max}$ by various factors; for example, SGx2 denotes the SG model using Y_0 and $Y_{wh, max}$ that are twice the nominal values. This is standard practice to provide a range of growth predictions that can explain experimental results.^{32,39}

The PTW model is a more advanced analytical formulation that has a built-in pressure and temperature dependence as well as their effects on the melting point. It has been successfully applied to many materials, including iron, through 14 material parameters, many of whom are rooted in the physical processes occurring during deformation. It is based on both thermally activated dislocation motion and drag-controlled kinetics. The constitutive equation describes yield stress as a function of pressure, temperature, and strain rate. The dependence of material strength on applied plastic strain at low strain rates is of the Arrhenius form; work hardening is modeled as a generalized Voce law.⁴⁰ At strain rates exceeding 10^9 s^{-1} , work hardening is neglected, and the rate dependence of the flow stress is calculated using Wallace’s theory of overdriven shocks in metals.⁶ The constitutive equation for the shear flow stress ($\hat{\tau}$), equal to half the von Mises stress [e.g., Eq. (2)] divided by the shear modulus, is

frequency, and β is determined experimentally. Parameters used for each model are listed in Table I where s_x and y_x are used in the calculation of $\hat{\tau}_s$ and $\hat{\tau}_y$, respectively.

B. Equation of state

The EOS of a material is required in computations to connect the conservation laws. Iron has multiple EOS models available, three of which are investigated here: LEOS 260,^{43,44} SESAME 2140,⁴⁵ and LEOS 263.⁴⁶ The SESAME and LEOS 263 models are

TABLE I. Parameters for iron for SG and PTW strength models.

Steinberg–Guinan ⁴¹		Preston–Tonks–Wallace ⁴²		
			α -Fe	ϵ -Fe
G_0 (GPa)	77	θ	0.015	0.015
G_p' (1/GPa)	226	p	3.0	3.0
G_T' (1/K)	4.55×10^{-5}	s_0	0.01	0.01
Y_0 (GPa)	0.34	s_∞	2.5×10^{-3}	2.5×10^{-3}
$Y_{wh,max}$ (GPa)	2.5	y_0	6.625×10^{-3}	6.625×10^{-3}
β	43	y_∞	7.5×10^{-4}	7.5×10^{-4}
ϵ_i	0	y_1	6.625×10^{-3}	0.03
n	0.35	y_2	0.265	0.25
		κ	0.35	0.3
		γ	1×10^{-5}	1×10^{-5}
		β	0.265	0.25
		α	0.23	0.23
		T_{melt} (K)	1810	2050
		G_0 (GPa)	87.2	87.2

multiphase forms that account for the high temperature and pressure solid-state phase changes in iron, while LEOS 260 does not distinguish between the various solid phases. The epsilon phase of iron extends from ~ 13 GPa to pressures well above 400 GPa;^{31,47} it has been proposed that at 350 GPa, there is a high-temperature body-centered cubic (bcc) phase of iron and it is that phase of iron in the Earth's inner core.⁴⁸ However, many other publications, both at low^{47,49–53} and high strain rates,^{31,54–58} find that the hcp phase is stable at core pressures and up until melt,⁵⁹ and the equations of state used here do not include a high-pressure bcc phase. The equations of state of the proposed bcc phase and the hexagonal epsilon phase are very similar, and the small differences have no effect on this design. Figure 1 shows the shock Hugoniot and melt curve for each model. There is little difference in the Hugoniots at low P–T conditions, but the models begin to deviate around 150 GPa. The melt temperature as a function of pressure is much lower for LEOS 263, meaning that it predicts melting at a lower temperature for a given pressure state.

C. Computational details

The direct-drive design reported here uses shaping of a laser pulse to drive a multilayer target, including ablator, pusher, sample, and tamper materials. The uniquely long (60 ns) laser pulse is only available at the NIF since it is the only facility with the capability of stitching together 16 beams. Furthermore, the NIF has incredibly fine control, both spatial and temporal, over the laser drives it can produce. The models used for each layer of material are listed in Table II where early simulations find that the thin applications of glue, typically $<3 \mu\text{m}$, used to adhere layers together are of negligible thickness and strength. The materials in the layers around iron have relatively low strength; therefore, no strength models are used for Be, BrCH, epoxy, or LiF. If a thick material with significant strength is used next to the iron ripples, then the experiment will not produce accurate results for iron strength. Unlike the case of pressure–shear loading experiments,⁶⁵ these materials and the glue

layers that bond them do not need to be strong enough to transmit the large shear stress that forms in the iron. Each material layer has a $0.5 \mu\text{m}$ mesh size except for the Be ablator, which has a finer ablative mesh to ensure that laser energy absorption is modeled correctly. A mesh convergence study was run in Ares to ensure that a $0.5 \mu\text{m}$ mesh is well converged—there is a $<5\%$ difference in the growth factor for a smaller mesh; therefore, it was concluded that this mesh size is enough to get reasonable growth factor predictions for a long enough run time (i.e., before mesh tangling ends the simulation). Boundary conditions are also applied to reduce

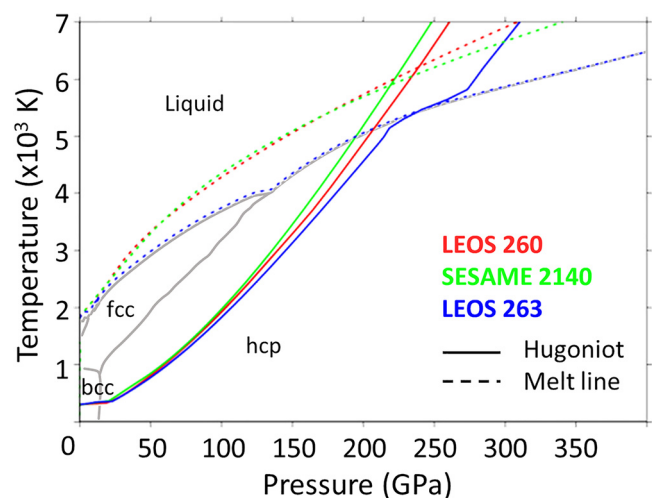


FIG. 1. Shock Hugoniot and melt curves for the three iron EOS models used. The solid–solid phase boundaries (gray) correspond to the newly developed LEOS 263 model (courtesy of Wu⁴⁸). The LEOS 263 phase boundaries and melt curves agree with data from various static^{60–62} and dynamic^{59,63,64} works.

TABLE II. Materials used in the simulations.

Material	Thickness (μm)	Density (g/cm^3)	EOS	Strength model
Be	70	1.858	LEOS 40	N/A
12.5% BrCH	75	2.0	LEOS 5128	N/A
Epoxy	20	1.185	LEOS 5030	N/A
Iron	50	7.877	LEOS 260	SG $\times 0, 1, 2, 5$
		7.85	SESAME 2140	α -PTW
		7.874	LEOS 263	ϵ -PTW
LiF	500	2.64	LEOS 2240	N/A

computational cost. The sides of the target are set such that they act as reflecting boundaries. The front of the target is set such that it remains fixed for the entirety of the simulation, and the back of the target is allowed to move freely.

III. RESULTS

A. Target design

The design of the target is based on previous experiments^{11,39} using beryllium (Be) as the ablator material, followed by 2%–12% brominated plastic (BrCH), which acts as the shield layer against x-rays generated by laser ablation that can heat the iron sample. The shield layer is followed by a low-density rippled epoxy, which

allows RT unstable ripples to grow by providing a relatively high Atwood number at the interface. Metal foams instead of an epoxy layer have also been postulated to be suitable, retaining a low-density post-shock compared to fully dense transition metals, but our simulations show that the foam's high shock temperature and thermal conductivity cause premature melting in the iron. The epoxy interfaces with the rippled iron foil, which is backed by lithium fluoride (LiF) that acts as a pressure tamper.

Since the role of the ablator is to produce a plasma that rapidly expands, causing a pressure wave to travel into the target, these simulations show that a thicker Be results in higher peak pressure and lower peak temperature in the iron (Fig. 2). The increased pressure is the result of pressure waves interacting and growing as they travel through thicker material. The lower temperature occurs because there is physically more material, which causes heat to dissipate more before reaching the next layer.

The x-ray/heat shield material is crucial in preventing unwanted heating in the iron due to x-rays. This ensures that any temperature increase is solely due to plastic work hardening and, therefore, related to material strength and comfortably below melting. The pressure is relatively insensitive to the BrCH thickness and the Br doping level (Fig. 2). The temperature, however, is sensitive to thicker BrCH or higher %Br. These two factors greatly reduce the temperature at the front of the iron as well as improve temperature stability. The higher-atomic number (Z) bromine increases opacity and restricts the transfer of energy (heat) throughout the material. An additional factor needs to be considered when a thicker heat shield is used: ripple radiography backlighter x-ray transmission for image plate data collection. A thicker heat shield

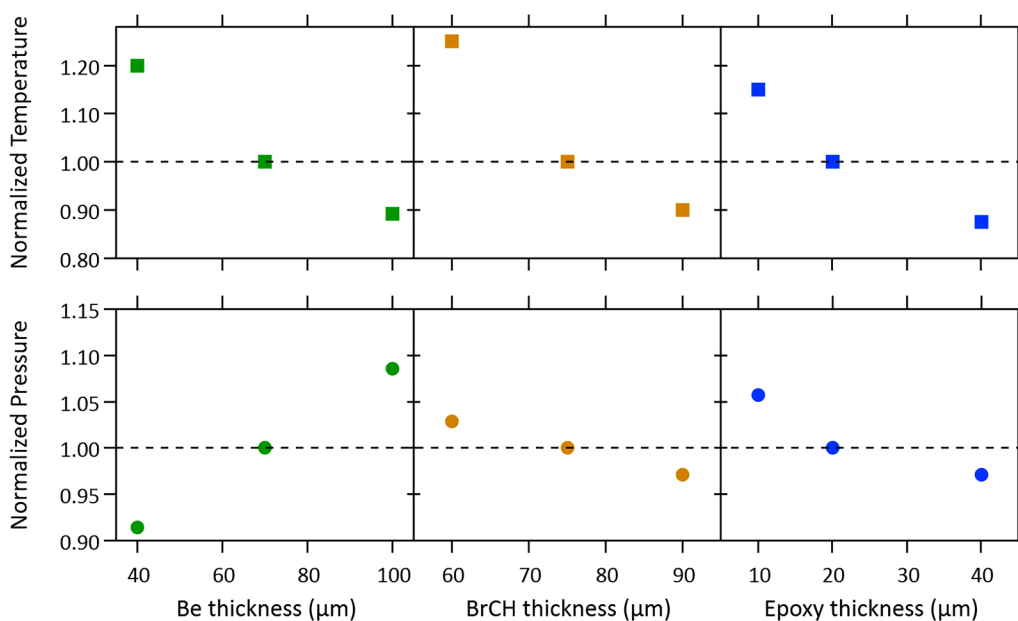


FIG. 2. Normalized pressure and temperature as a function of material thickness where a normalized value of 1 corresponds to $P = 350$ GPa and $T = 4000$ K. Variations in material thickness shown here are representative of all the options that were simulated for this work.

or higher %Br has the effect of decreasing the transmission of the backlighter x-rays—impeding the radiography signal level.

The use of thicker rippled epoxy (10–40 μm) improves the overall pressure behavior, resulting in fewer reverberations. If a pressure wave interacts with a boundary where the sound impedance changes, wave reflections and interactions are generated. For a thinner epoxy layer, the front and back boundaries are close to each other, and the various pressure waves are reflected and interact much more, causing large reverberations. A thicker version simply allows some of the reflected waves to dissipate, lessening and delaying the pressure jumps. A thicker epoxy layer also causes lower temperature in the iron due to heat dissipation effects (Fig. 2).

B. Pulse shape design

The laser pulse shape ramps up in power to help ensure the iron does not melt before reaching the desired P–T conditions. Three aspects of the pulse shape were investigated—initial shock-inducing jump, picket addition, and “hold” time. Inducing a shock at the beginning of the pulse is an easy way to initialize the sample into a specific P–T state along the Hugoniot to reach more extreme conditions. Since a shock generates on-Hugoniot compression, the temperature can be easily predicted; i.e., an initial shock of 100 GPa should increase temperature to ~ 2000 K. A picketed pulse is set by dropping the laser power after an initial shock pulse. The picket pulse is timed in such a way to destructively interfere with

reverberations from sample interfaces. Including a picket reduces the severity of the pressure drop at early time as well as causing a slight reduction of temperature at the iron front. It is important that the picket does not cause the iron to revert to the α phase (<13 GPa), avoiding unnecessary phase transitions. This is accomplished by keeping the laser power after the post-picket power drop to above 0.03 TW. Lastly, the late time “hold,” which is a monotonic increase in power, is used to create a stable region in time at the desired pressure. A longer “hold” results in more time at peak pressure but also causes significantly more heating (and premature melting). By using a 60 ns pulse shape, rather than 30 ns, the peak pressure can be held for longer time and the ramped portion can be more gradual, allowing for more time during which $T/T_m < 1$. This is the only feasible way to make a solid-state iron strength measurement at the extremely high pressure and high temperature of interest.

The optimized target and the pulse shape design are shown in Fig. 3. The target consists of a 70 μm Be ablator, a 75 μm 12.5% BrCH heat shield, 20 μm epoxy, 50 μm iron, and 500 μm LiF. The pulse is made up of a 6 ns 0.2 TW picket, drop to ~ 0.1 TW, ramp, and “hold” to a peak power of 2 TW. In the experiments, this pulse is delivered to the target by 16 NIF beams [Fig. 3(a)]. At a prescribed delay time, a separate set of 12 NIF beams illuminates a thin foil, which causes x-rays to be emitted and backlight the ripple target for face-on radiography. The desired 350 GPa pressure state is maintained for ~ 10 ns [Fig. 4(a)], while the ideal 5000 K

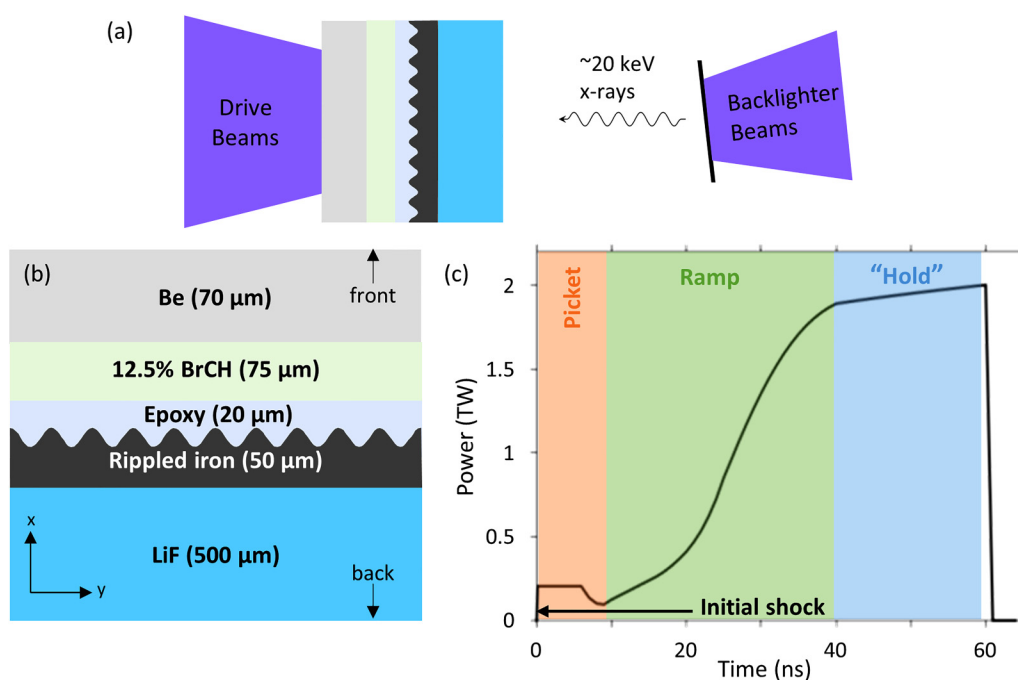


FIG. 3. (a) Experimental configuration, where the sample is compressed by a set of NIF laser beams. The ripple growth is measured with face-on radiography from laser illumination of a backlighter foil to produce x-rays. Backlighter energy is dependent on foil material. Optimized (b) target and (c) pulse shape designs. The epoxy is applied directly to the iron ripples. The other layers are joined by thin ($<3\mu\text{m}$) layers of epoxy (not shown) that have no effect on the growth factor in the RT design simulations.

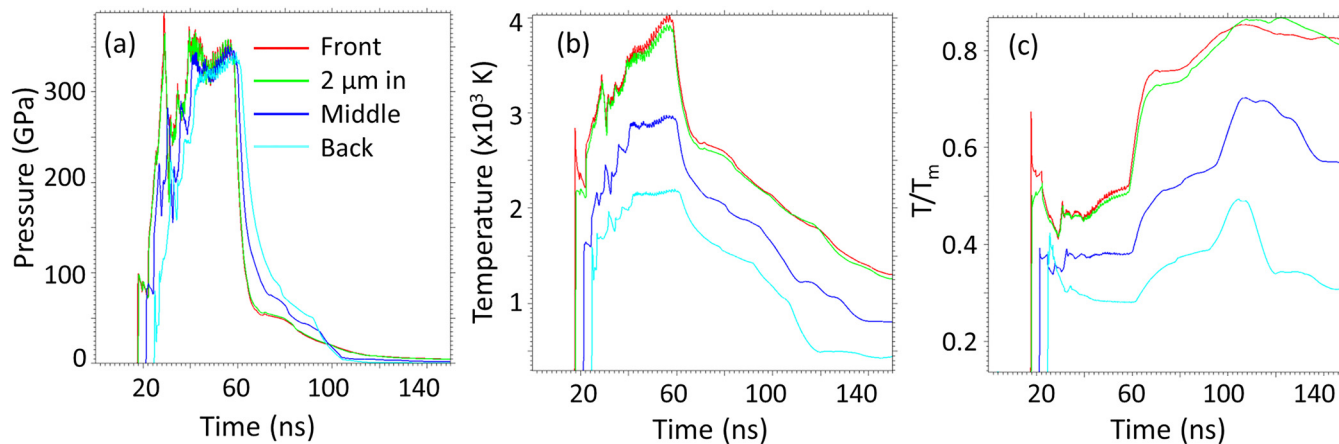


FIG. 4. Hydra simulations of (a) pressure, (b) temperature, and (c) T/T_m in the iron at different locations. Red, green, blue, and teal curves correspond to various locations in the iron layer: front (rippled face), $2\mu\text{m}$ in, middle, and back, respectively.

temperature condition is not quite achieved. A peak temperature of 4000 K is reached for a few nanoseconds [Fig. 4(b)]. The iron also remains in the solid state ($T/T_m < 1$) for the entirety of the simulation [Fig. 4(c)]. Experimentally, the measurement will be made at peak pressure, between 50 and 60 ns.

C. Strength and EOS effects

The effect of strength on the RT instability was investigated with 2D Ares simulations (Fig. 5). By introducing a sinusoidal ripple pattern onto the front surface of the iron, the effect of

strength can be inferred by measuring the growth factor (GF). The growth factor is essentially the ratio of the final and initial ripple areal density, that is, the multiplication of amplitudes by density. In practice, blurring of the ripple image in the experiment due to geometry and other factors must be accounted for by dividing GF by the modulation transfer function.⁶⁶ The simulations predict values for the von Mises flow stress, while experimental RT measurements are a measure of the flow stress (half the von Mises stress⁶). For a $1\mu\text{m}$ amplitude and a $75\mu\text{m}$ wavelength ripple pattern, the peak growth factor for iron with different levels of strength varies from 3 to 10 (Fig. 6). Growth factors in this range

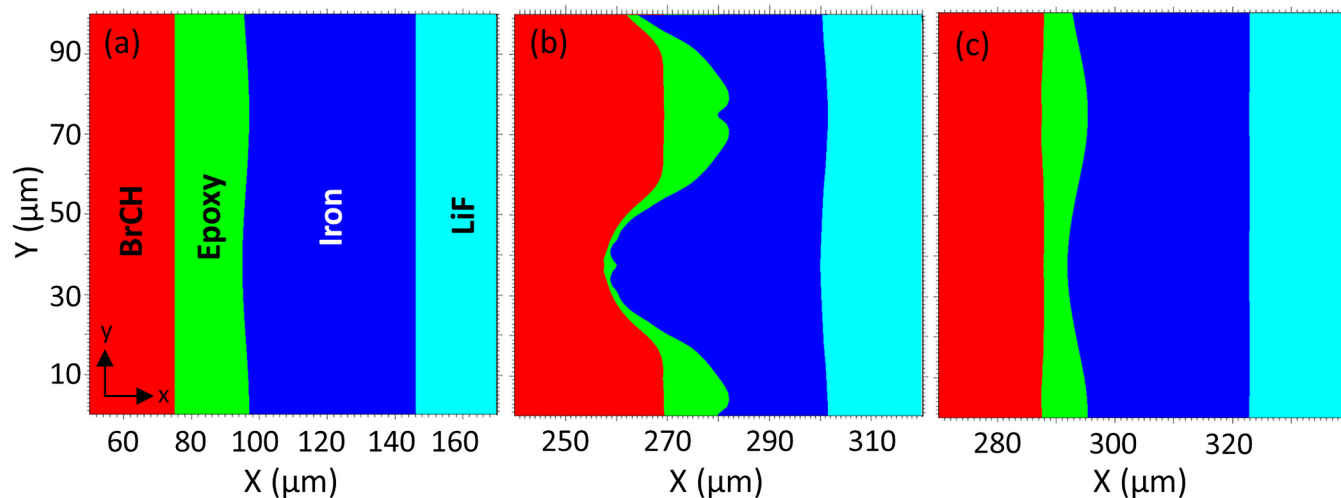


FIG. 5. Ripple growth time sequence starting at (a) $t=0$ with an initial ripple pattern of $1\mu\text{m}$ amplitude and $75\mu\text{m}$ wavelength. Late time ripple growth ($t \sim 55\text{ ns}$) for (b) no strength and (c) high strength ($\text{SG} \times 5$) cases assuming an LEOS 260 model. Material layers are BrCH (red), epoxy (green), Fe (blue), and LiF (aqua). BrCH and LiF layers are cropped for a better view of ripple growth.

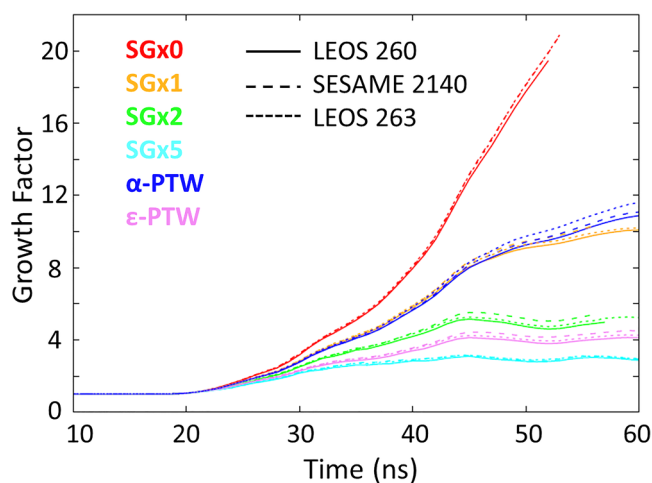


FIG. 6. Growth factor calculations using 2D Ares for $1\ \mu\text{m}$ amplitude/ $75\ \mu\text{m}$ wavelength ripples in iron with different strength models (indicated by color) and EOS tables (indicated by line style).

will provide a robust signal to noise in the collected radiography data. Here, SGx0,1,2,5 multipliers refer to multiplying the Y_0 parameter and maximum yield strength from work hardening ($Y_{wh,max}$) by the specified scale factor essentially scaling the flow stress. The 0 multiplier represents a no-strength case. In a no-strength case, the iron behaves like a liquid, and the perturbations exhibit classical, or uninhibited, RT growth. In this case, the growth rate is proportional to the square root of the Atwood number ($\gamma = \sqrt{Aka}$, where k is the wavenumber or $1/\text{wavelength}$ and a is the acceleration so that $GF = e^{\gamma t}$ in classical growth). The original SG and α -PTW strength models predict similar growth behavior—peaking at $GF \sim 10$. The ϵ -PTW model⁴² with $GF \sim 4$ is constructed to give the strength of the high-pressure phase and is expected theoretically to best predict experimental results. $2\times$ and $5\times$ multipliers of the original SG model also predict less growth, indicating even higher iron strength. The range of growth factors predicted here corresponds to strengths ranging from 3 to 30 GPa at a strain rate of $\sim 5 \times 10^6\ \text{s}^{-1}$, with the ideal ϵ -PTW model predicting strength of 5 GPa [much lower than the value found by Huntington *et al.* ($>40\ \text{GPa}$)²²]. Note that those RT experiments were carried out at lower pressure (150 GPa) and likely lower temperature (not reported).

The equation of state, or more specifically the melt curve associated with it, can also have a pronounced effect in predictions of the growth factor because depending on the model, T/T_m can be greater than 1 at different times. The melt curve of LEOS 263 lies at higher pressures than that of the other EOS tables used (Fig. 1), meaning the iron melts at lower temperature and potentially, earlier time. If the iron sample were to melt at an earlier time, the growth factor would follow the classical zero strength case and be much higher. Designing the target in such a way to make sure the sample does not melt until late in time helps to ensure we are taking an accurate solid-state strength measurement at the desired P–T conditions. The predicted ripple growth based on the EOS

table used does not vary greatly (Fig. 6), and the predicted yield strength and strain rate at a given time are similar between EOS models.

IV. CONCLUSIONS

We have described the computational design work for high-pressure iron Rayleigh–Taylor strength experiments at the NIF. The lack of clear experimental results on iron strength at high pressure and temperature conditions comparable to the Earth’s inner core motivates these direct-drive shots, which need extensive design as they have never been attempted before. Design work for the high-power direct-drive laser experiments is a complicated process of carefully balancing target components and pulse shape with the physical limitations of target fabrication and power limitations of the laser facility. The target components and pulse shape were optimized to produce the desired high pressure and temperature conditions. These extreme conditions require a design that induces a solid-solid phase transformation in the iron and take it to temperatures that approach melt. The effect of various strength models and EOS tables on ripple growth was investigated to predict experimental results and accommodate the large theoretical uncertainty in the iron strength. Growth factors of 3–10 are predicted based on the optimal target and pulse shape with minimal variation based on the EOS used.

The desired pressure state in the iron is achieved using a picketed pulse followed by a smooth ramp and a “hold” up to 2 TW peak power. This design is the first example of how a longer (60 ns) pulse provides improved design options. Pressure is relatively insensitive to changes in target layer thicknesses, while temperature is highly variable. The P–T state of 350 GPa and 4000 K in the iron is achieved using a beryllium ablator ($70\ \mu\text{m}$), brominated plastic heat shield ($75\ \mu\text{m}$), epoxy pusher ($20\ \mu\text{m}$), and lithium fluoride tamper ($500\ \mu\text{m}$). Thinner layers before the iron can help to reach even higher temperatures but with a trade-off of the stability of the temperature state. Higher peak power in the pulse shape can also increase temperature, but with a danger of premature melting as well as power limitations of the NIF laser beams. Similar principles are applied to design Omega EP RT strength experiments where different peak temperatures can be achieved by changing the strength of the initial shock-inducing power jump in the pulse shape. This uniquely optimized design will be able to provide strength measurements of iron at extreme conditions adding to high-pressure materials science and providing iron data in a regime where the paucity of data to inform geo-physical models is acute.

ACKNOWLEDGMENTS

We appreciate the support provided by LLNL ACT-UP (Sub-contract No. B639114) and the Center for Matter under Extreme Conditions (DOE NNSA Grant No. DE-NA0003842), which made this research program possible. We also acknowledge the NIF Discovery Science project and the Omega EP LaserNetUS project for the experimental facilities that are being used in conjunction with these computational predictions. The work of T.E.L., R.E.R., and H.S.P was supported by the U.S. Department of

Energy, Lawrence Livermore National Laboratory, under Contract No. DE-AC52-07NA27344. This document has been released under LLNL-JRNL-830377.

AUTHOR DECLARATIONS

Conflict of Interest

The authors have no conflicts to disclose.

DATA AVAILABILITY

The data that support the findings of this study are available from the corresponding author upon reasonable request.

REFERENCES

- ¹B. A. Buffett, "Dynamics of the Earth's core," in *Earth's Deep Interior: Mineral Physics and Tomography from the Atomic to the Global Scale* [American Geophysical Union (AGU), 2013], pp. 37–62.
- ²R. Jeanloz, "The nature of the Earth's core," *Annu. Rev. Earth Planet. Sci.* **18**, 357–386 (1990).
- ³H. Mao *et al.*, "Elasticity and rheology of iron above 220 GPa and the nature of the Earth's inner core," *Nature* **396**, 741–743 (1998).
- ⁴A. H. Cottrell, "Commentary," in *A Brief View of Work Hardening*, edited by F. R. N. Nabarro and M. S. Duesbery (Elsevier, 2002), Vol. 11, pp. vii–xvii.
- ⁵G. R. Johnson and W. H. Cook, "A constitutive model and data for metals subjected to large strains, high strain rates and high temperatures," in *Proceedings 7th International Symposium on Ballistics* (The Hague, The Netherlands, 1983), pp. 541–547.
- ⁶D. L. Preston, D. L. Tonks, and D. C. Wallace, "Model of plastic deformation for extreme loading conditions," *J. Appl. Phys.* **93**, 211–220 (2003).
- ⁷L. J. W. S. Rayleigh, "Investigation of the character of the equilibrium of an incoming pressibly heavy fluid of variable density," *Proc. London Math. Soc.* **14**, 170–177 (1883).
- ⁸G. I. Taylor, "The instability of liquid surfaces when accelerated in a direction perpendicular to their planes," *Int. Proc. R. Soc. London Ser. Math. Phys. Sci.* **201**, 192–196 (1950).
- ⁹H.-S. Park *et al.*, "Strong stabilization of the Rayleigh–Taylor instability by material strength at megabar pressures," *Phys. Plasmas* **17**, 056314 (2010).
- ¹⁰H.-S. Park *et al.*, "Viscous Rayleigh–Taylor instability experiments at high pressure and strain rate," *Phys. Rev. Lett.* **104**, 135504 (2010).
- ¹¹H.-S. Park *et al.*, "Experimental results of tantalum material strength at high pressure and high strain rate," *AIP Conf. Proc.* **1426**, 1371–1374 (2012).
- ¹²S. Fujioka *et al.*, "Suppression of the Rayleigh–Taylor instability due to self-radiation in a multiablation target," *Phys. Rev. Lett.* **92**, 195001 (2004).
- ¹³L. Masse, "Stabilizing effect of anisotropic thermal diffusion on the ablative Rayleigh–Taylor instability," *Phys. Rev. Lett.* **98**, 245001 (2007).
- ¹⁴A. Sunahara, J. A. Delettrez, C. Stoeckl, R. W. Short, and S. Skupsky, "Time-dependent electron thermal flux inhibition in direct-drive laser implosions," *Phys. Rev. Lett.* **91**, 095003 (2003).
- ¹⁵E. Ott and D. A. Russell, "Diffuse-boundary Rayleigh–Taylor instability," *Phys. Rev. Lett.* **41**, 1048–1051 (1978).
- ¹⁶A. B. Bud'ko and M. A. Liberman, "Suppression of the Rayleigh–Taylor instability by convection in ablatively accelerated laser targets," *Phys. Rev. Lett.* **68**, 178–181 (1992).
- ¹⁷V. Lobatchev and R. Betti, "Ablative stabilization of the deceleration phase Rayleigh–Taylor instability," *Phys. Rev. Lett.* **85**, 4522–4525 (2000).
- ¹⁸R. Betti, V. N. Goncharov, R. L. McCrory, and C. P. Verdon, "Self-consistent cutoff wave number of the ablative Rayleigh–Taylor instability," *Phys. Plasmas* **2**, 3844–3851 (1995).
- ¹⁹H. Takabe, K. Mima, L. Montierth, and R. L. Morse, "Self-consistent growth rate of the Rayleigh–Taylor instability in an ablatively accelerating plasma," *Phys. Fluids* **28**, 3676 (1985).
- ²⁰S. M. Gol'berg and A. L. Velikovich, "Suppression of Rayleigh–Taylor instability by the snowplow mechanism," *Phys. Fluids B: Plasma Phys.* **5**, 1164–1172 (1993).
- ²¹J. F. Barnes, P. J. Blewett, R. G. McQueen, K. A. Meyer, and D. Venable, "Taylor instability in solids," *J. Appl. Phys.* **45**, 727–732 (1974).
- ²²C. M. Huntington *et al.*, "Investigating iron material strength up to 1 Mbar using Rayleigh–Taylor growth measurements," *AIP Conf. Proc.* **1793**, 110007 (2017).
- ²³Omega Laser Facility—Laboratory for Laser Energetics, see <https://www.lle.rochester.edu/index.php/omega-laser-facility-2/>.
- ²⁴NIF and Photon Science, see <https://lasers.llnl.gov/>.
- ²⁵V. Gandhi, S. Ravindran, and G. Ravichandran, "Dynamic strength of iron at high pressures and strain rates," *Phys. Rev. Lett.* **128**, 015705 (2022).
- ²⁶A. E. Gleason and W. L. Mao, "Strength of iron at core pressures and evidence for a weak Earth's inner core," *Nat. Geosci.* **6**, 571–574 (2013).
- ²⁷Y. Ping *et al.*, "Solid iron compressed up to 560 GPa," *Phys. Rev. Lett.* **111**, 065501 (2013).
- ²⁸S. Merkel *et al.*, "Femtosecond visualization of hcp-iron strength and plasticity under shock compression," *Phys. Rev. Lett.* **127**, 205501 (2021).
- ²⁹J. Lindl, "Development of the indirect-drive approach to inertial confinement fusion and the target physics basis for ignition and gain," *Phys. Plasmas* **2**, 3933–4024 (1995).
- ³⁰J. D. Moody *et al.*, "Progress in hohlraum physics for the National Ignition Facility," *Phys. Plasmas* **21**, 056317 (2014).
- ³¹J. Wang *et al.*, "Ramp compression of iron to 273 GPa," *J. Appl. Phys.* **114**, 023513 (2013).
- ³²B. A. Remington *et al.*, "Rayleigh–Taylor instabilities in high-energy density settings on the National Ignition Facility," *Proc. Natl. Acad. Sci. U.S.A.* **116**, 18233–18238 (2019).
- ³³A. Krygier *et al.*, "Extreme hardening of Pb at high pressure and strain rate," *Phys. Rev. Lett.* **123**, 205701 (2019).
- ³⁴J. Colvin and J. Larsen, *Extreme Physics: Properties and Behavior of Matter at Extreme Conditions* (Cambridge University Press, 2013).
- ³⁵Lawrence Livermore National Laboratory, "Inertial confinement fusion quarterly report," April–June 1995, Vol. 5, No. 3, UCRL-LR-105821-95-3, 187252; see <http://www.osti.gov/servlets/purl/187252-A14f18/webviewable/>.
- ³⁶G. Bazan, "ASCI code calculations of 3D supernova hydrodynamic instabilities," in *193rd AAS Meeting Abstracts* (American Astronomical Society, 1999), vol. 31, p. 669, id. 124–09.
- ³⁷D. J. Steinberg, S. G. Cochran, and M. W. Guinan, "A constitutive model for metals applicable at high-strain rate," *J. Appl. Phys.* **51**, 1498–1504 (1980).
- ³⁸D. J. Steinberg and C. M. Lund, "A constitutive model for strain rates from 10^{-4} to 10^6 s $^{-1}$," *J. Appl. Phys.* **65**, 1528–1533 (1989).
- ³⁹K. O. Mikaelian, "Design of a Rayleigh–Taylor experiment to measure strength at high pressures," *Phys. Plasmas* **17**, 092701 (2010).
- ⁴⁰E. Voce, "The relationship between stress and strain for homogeneous deformation," *J. Inst. Met.* **74**, 537 (1948).
- ⁴¹D. J. Steinberg, *Equation of State and Strength Properties of Selected Materials* (Lawrence Livermore National Laboratory, 1996).
- ⁴²J. L. Belof *et al.*, "Rayleigh–Taylor strength experiments of the pressure-induced $\alpha \rightarrow \epsilon \rightarrow \alpha'$ phase transition in iron," *AIP Conf. Proc.* **1426**, 1521–1524 (2012).
- ⁴³R. M. More, K. H. Warren, D. A. Young, and G. B. Zimmerman, "A new quotidian equation of state (QEOS) for hot dense matter," *Phys. Fluids* **31**, 3059 (1988).
- ⁴⁴D. A. Young and E. M. Corey, "A new global equation of state model for hot, dense matter," *J. Appl. Phys.* **78**, 3748–3755 (1995).
- ⁴⁵G. I. Kerley, "Multiphase equation of state for iron," SAND-93-0027, 6345571, 1993; see <http://www.osti.gov/servlets/purl/6345571/>.
- ⁴⁶C. J. Wu, LEOS 263 (unpublished) (2022).

- ⁴⁷G. Shen, H. Mao, R. J. Hemley, T. S. Duffy, and M. L. Rivers, "Melting and crystal structure of iron at high pressures and temperatures," *Geophys. Res. Lett.* **25**, 373–376, <https://doi.org/10.1029/97GL03776> (2022).
- ⁴⁸A. B. Belonoshko *et al.*, "Stabilization of body-centred cubic iron under inner-core conditions," *Nat. Geosci.* **10**, 312–316 (2017).
- ⁴⁹Y. Ma *et al.*, "In situ x-ray diffraction studies of iron to Earth-core conditions," *Phys. Earth Planet. Inter.* **143–144**, 455–467 (2004).
- ⁵⁰Y. Kuwayama, K. Hirose, N. Sata, and Y. Ohishi, "Phase relations of iron and iron–nickel alloys up to 300 GPa: Implications for composition and structure of the Earth's inner core," *Earth Planet. Sci. Lett.* **273**, 379–385 (2008).
- ⁵¹S. Tateno, K. Hirose, Y. Ohishi, and Y. Tatsumi, "The structure of iron in Earth's inner core," *Science* **330**, 359–361 (2010).
- ⁵²A. Dewaele *et al.*, "Mechanism of the α - ϵ phase transformation in iron," *Phys. Rev. B* **91**, 174105 (2015).
- ⁵³S. Merkel, A. Lincot, and S. Petitgirard, "Microstructural effects and mechanism of bcc-hcp-bcc transformations in polycrystalline iron," *Phys. Rev. B* **102**, 104103 (2020).
- ⁵⁴B. Branch and B. J. Jensen, "Dynamic x-ray diffraction to study the shock-induced α - ϵ phase transition in iron," *AIP Conf. Proc.* **1979**, 040001 (2018).
- ⁵⁵A. Denoed *et al.*, "Dynamic X-ray diffraction observation of shocked solid iron up to 170 GPa," *Proc. Natl. Acad. Sci. U.S.A.* **113**, 7745–7749 (2016).
- ⁵⁶J. A. Hawreliak and S. J. Turneaure, "Probing the lattice structure of dynamically compressed and released single crystal iron through the alpha to epsilon phase transition," *Appl. Phys.* **129**, 135901 (2021).
- ⁵⁷D. H. Kalantar *et al.*, "Direct observation of the α - ϵ transition in shock-compressed iron via nanosecond x-ray diffraction," *Phys. Rev. Lett.* **95**, 075502 (2005).
- ⁵⁸B. Yaakobi *et al.*, "EXAFS measurement of iron bcc-to-hcp phase transformation in nanosecond-laser shocks," *Phys. Rev. Lett.* **95**, 075501 (2005).
- ⁵⁹S. J. Turneaure, S. M. Sharma, and Y. M. Gupta, "Crystal structure and melting of Fe shock compressed to 273 GPa *in situ* x-ray diffraction," *Phys. Rev. Lett.* **125**, 215702 (2020).
- ⁶⁰G. Morard *et al.*, "Solving controversies on the iron phase diagram under high pressure," *Geophys. Res. Lett.* **45**, 11,074, <https://doi.org/10.1029/2018GL079950> (2018).
- ⁶¹S. Anzellini, A. Dewaele, M. Mezouar, P. Loubeyre, and G. Morard, "Melting of iron at Earth's inner core boundary based on fast x-ray diffraction," *Science* **340**, 464–466 (2013).
- ⁶²R. Boehler, "Temperatures in the Earth's core from melting-point measurements of iron at high static pressures," *Nature* **363**, 534–536 (1993).
- ⁶³J. Li *et al.*, "Shock melting curve of iron: A consensus on the temperature at the Earth's inner core boundary," *Geophys. Res. Lett.* **47**, e2020GL087758, <https://doi.org/10.1029/2020GL087758> (2020).
- ⁶⁴M. Harmand *et al.*, "X-ray absorption spectroscopy of iron at multimegabar pressures in laser shock experiments," *Phys. Rev. B* **92**, 024108 (2015).
- ⁶⁵L. C. Chhabildas and J. W. Swegle, "Dynamic pressure-shear loading of materials using anisotropic crystals," *J. Appl. Phys.* **51**, 4799–4807 (1980).
- ⁶⁶J. F. Seely, G. E. Holland, L. T. Hudson, and A. Henins, "X-ray modulation transfer functions of photostimulable phosphor image plates and scanners," *Appl. Opt.* **47**, 5753 (2008).